



Year: 2019

Targeted photoredox catalysis in cancer cells

Huang, Huaiyi ; Banerjee, Samya ; Qiu, Kangqiang ; Zhang, Pingyu ; Blacque, Olivier ; Malcomson, Thomas ; Paterson, Martin J ; Clarkson, Guy J ; Staniforth, Michael ; Stavros, Vasilios G ; Gasser, Gilles ; Chao, Hui ; Sadler, Peter J

Abstract: Hypoxic tumours are a major problem for cancer photodynamic therapy. Here, we show that photoredox catalysis can provide an oxygen-independent mechanism of action to combat this problem. We have designed a highly oxidative Ir(III) photocatalyst, [Ir(ttpy)(pq)Cl]PF₆ ([1]PF₆, where 'ttpy' represents 4'-(p-tolyl)-2,2':6',2''-terpyridine and 'pq' represents 3-phenylisoquinoline), which is phototoxic towards both normoxic and hypoxic cancer cells. Complex 1 photocatalytically oxidizes 1,4-dihydronicotinamide adenine dinucleotide (NADH)-an important coenzyme in living cells-generating NAD center dot radicals with a high turnover frequency in biological media. Moreover, complex 1 and NADH synergistically photoreduce cytochrome c under hypoxia. Density functional theory calculations reveal pi stacking in adducts of complex 1 and NADH, facilitating photoinduced single-electron transfer. In cancer cells, complex 1 localizes in mitochondria and disrupts electron transport via NADH photocatalysis. On light irradiation, complex 1 induces NADH depletion, intracellular redox imbalance and immunogenic apoptotic cancer cell death. This photocatalytic redox imbalance strategy offers a new approach for efficient cancer phototherapy.

DOI: <https://doi.org/10.1038/s41557-019-0328-4>

Posted at the Zurich Open Repository and Archive, University of Zurich

ZORA URL: <https://doi.org/10.5167/uzh-178822>

Journal Article

Accepted Version

Originally published at:

Huang, Huaiyi; Banerjee, Samya; Qiu, Kangqiang; Zhang, Pingyu; Blacque, Olivier; Malcomson, Thomas; Paterson, Martin J; Clarkson, Guy J; Staniforth, Michael; Stavros, Vasilios G; Gasser, Gilles; Chao, Hui; Sadler, Peter J (2019). Targeted photoredox catalysis in cancer cells. *Nature Chemistry*, 11(11):1041-1048.

DOI: <https://doi.org/10.1038/s41557-019-0328-4>

Targeted photoredox catalysis in cancer cells

Huaiyi Huang^{1,2}, Samya Banerjee², Kangqiang Qiu³, Pingyu Zhang⁴, Olivier Blacque⁵, Thomas Malcomson⁶, Martin J. Paterson⁶, Guy J. Clarkson², Michael Staniforth², Vasilios G. Stavros², Gilles Gasser^{7*}, Hui Chao^{3*} and Peter J. Sadler^{2*}

¹School of Pharmaceutical Science (Shenzhen), Sun Yat-sen University, Guangzhou, 510275, China

²Department of Chemistry, University of Warwick, Coventry, CV4 7AL, UK

³MOE Key Laboratory of Bioinorganic and Synthetic Chemistry, School of Chemistry, Sun Yat-sen University, Guangzhou, 510275, China

⁴College of Chemistry and Environmental Engineering, Shenzhen University, Shenzhen, 518060, China

⁵Department of Chemistry, University of Zurich, Zurich, CH-8057, Switzerland

⁶School of Engineering and Physical Sciences, Heriot-Watt University, Edinburgh, EH4 4AS, UK

⁷Chimie ParisTech, PSL University, CNRS, Institute of Chemistry for Health and Life Sciences, Laboratory for Inorganic Chemical Biology, Paris, F-75005, France

These authors contributed equally: Huaiyi Huang and Samya Banerjee

Hypoxic tumours are a major problem for cancer photodynamic therapy. Here we show that photo-redox catalysis can provide an oxygen-independent mechanism of action to combat this problem. We have designed a highly oxidative Ir(III) photo-catalyst, [Ir(ttpy)(pq)Cl]PF₆ ([1]PF₆, ttpy = 4'-(p-tolyl)-2,2':6',2''-terpyridine, pq = 3-phenylisoquinoline), which is photo-toxic towards both normoxic and hypoxic cancer cells. Complex **1** photo-catalytically

oxidizes nicotinamide adenine dinucleotide (NADH), an important coenzyme in living cells, generating NAD^\bullet radicals with high turnover frequency in biological media. Moreover, complex **1** and NADH synergistically photo-reduce cytochrome c under hypoxia. Density functional theory calculations reveal π -stacking in adducts of **1** and NADH, facilitating photo-induced single electron transfer. In cancer cells, **1** localizes in mitochondria and disrupts electron transport via NADH photo-catalysis. Upon light irradiation, **1** induces NADH depletion, intracellular redox imbalance, and immunogenic-apoptotic cancer cell death. This photo-catalytic redox imbalance strategy offers a new approach for efficient cancer phototherapy.

Platinum compounds are the most widely used anticancer drugs in the clinic¹. However, new generations of metal-based anticancer agents are urgently needed to combat drug resistance and reduce side-effects^{2,3}. Photo-activated metal complexes can provide both temporal and spatial control over drug activation and show remarkable potential for cancer treatment⁴⁻⁸. Tin, lutetium, palladium and ruthenium based photosensitizers (PSs) are, or were, currently in clinical trials for cancer photodynamic therapy (PDT)^{9,10}. The catalytic nature of PDT can achieve high therapeutic efficacy at low doses¹¹, and, in general, does not show cross resistance to chemotherapy, helpful for overcoming drug resistance¹². However, a few cases of clinical resistance to PSs are emerging¹³⁻²¹. The mechanisms of PDT resistance include hypoxia¹³, detoxification by intracellular antioxidants systems,^{14,15} induction of stress response genes,¹⁶⁻²⁰ and drug efflux by P-glycoprotein²¹. These considerations indicate the urgency of developing new generations of PSs and novel mechanisms of action (MOA) for cancer phototherapy. The high dependence of the MOA of PDT on oxygen restricts its application, since cancer cells grow mostly under hypoxia²². We have therefore investigated novel PSs with new MOAs against hypoxic cancer cells.

Although most tumours adopt a Warburg-type glycolytic metabolism, Reactive Oxygen Species (ROS) released from the mitochondrial electron transport chain (ETC) are essential for cell proliferation and redox regulatory functions of cancer cells under hypoxia²³. The electron source in the ETC is 1,4-dihydronicotinamide adenine dinucleotide (NADH, Fig.

1a), which participates in the maintenance of the intracellular redox balance and as a coenzyme in >400 oxidoreductases²⁴. We hypothesise that selective induction of NADH depletion and of ETC disruption in cancer cells may destroy the intracellular redox balance and kill cancer cells under hypoxia.

Photo-catalysts which induce single electron transfer (SET) between substrates have achieved great success in organic synthesis²⁵. It is notable that most reported photoredox catalysis has been carried out in degassed organic solvents²⁶. An oxygen-independent MOA is appealing for NADH photo-catalysis in hypoxic cancer cells. However, strong triplet excited-state quenching by water and oxygen severely limits the application of traditional photo-catalysts in biological systems²⁷.

Here we have synthesised and characterised a novel stable iridium photo-catalyst (**1**, Fig. 1b) with an unusually high excited state redox potential compared to common PSs²⁵. Strikingly, upon light irradiation in biological media, complex **1** shows more than two orders of magnitude higher NADH turnover frequency (TOF) than organometallic half-sandwich catalysts²⁸. Moreover, **1** can photo-catalyse cytochrome c (cyt c) reduction in the presence of NADH under hypoxia. We have carried out detailed experimental and computational studies on photo-catalytic NADH oxidation in aqueous media, involving the trapping of NAD[•] radicals and their characterisation. In addition, complex **1** targets mitochondria in cancer cells, and, importantly, shows almost equivalent photo-cytotoxicity under normoxia and hypoxia, as well as low toxicity to unirradiated normal cells.

Results

Photosensitizer design and characterisation

Complex **1** was characterised by analytical and spectroscopic data, and x-ray crystallography (Fig. 1c, Supplementary Tables 1, 2). Ir(III) photoredox catalysts with bidentate ligands often exist as a mixture of enantiomers²⁹. The incorporation of tridentate ligands can avoid chirality³⁰, as in the present case (Fig. 1c). Density functional theory (DFT) calculations confirmed that the

trans C-Cl isomer found in the crystal structure is 33.5 kJ mol⁻¹ more stable than the *cis* C-Cl isomer. Complex **1** showed absorption between 350-480 nm (Supplementary Fig. 1), which matched well with spectra calculated by time-dependent DFT (TD-DFT; Supplementary Fig. 2), with low-lying metal-to-ligand charge-transfer states (MLCT, Supplementary Table 3).

The phosphorescence of complex **1** was sensitive to solvent polarity (Supplementary Fig.3, Supplementary Table 4) with emission at ca. 562 nm similar to the calculated data (567 nm, Supplementary Table 3) at 293 K. Moreover, oxygen strongly influenced the phosphorescence intensity and lifetime of **1** (Supplementary Figs. 4,5, Supplementary Table 4), being longer in acetonitrile (743.7/1390.3 ns, air/N₂) than in phosphate buffered saline (PBS, 330.8/382.3 ns, air/N₂). The lowest energy singlet excited state S₁ arises from LUMO ← HOMO excitation and showed both ligand-to-ligand charge-transfer ¹LL(C[^]N→tppy)CT and MLCT character (Supplementary Table 3, Supplementary Fig. 6). Upon light excitation, the excited triplet transition “hole” (Fig. 2a) is localised on the π-system of the C[^]N ligand, while the “particle” is localised on the N[^]N[^]N ligand. In addition, complex **1** exhibited strong two-photon absorption (TPA) (Fig. 2b), observed with a maximum at ca. 760 nm (Supplementary Fig. 7) and a two-photon absorption cross section of 160 Goeppert-Mayer (GM).

Ideally, efficient photo-catalytic drugs should exhibit high dark- and photo-stability. Complex **1** showed excellent stability in both organic solvents, e.g. DMSO (Supplementary Fig. 8), RPMI-1640 cell culture medium (Fig. 2c), and human serum (Supplementary Fig. 9) on prolonged incubation. Additionally, **1** also exhibited no photo-degradation under 463 nm blue-light irradiation in PBS (Fig. 2d).

Cyclic voltammetry revealed a significantly different redox behavior in the ground and excited states of **1** (Supplementary Table 5). The excited-state redox potential of **1** ($E_{1/2}^{*III/II} = +1.22$ V vs SCE, $E_{1/2}^{IV/*III} = -0.48$ V vs SCE) is higher than for reported Ru(II) or Ir(III)

photocatalysts (Supplementary Fig. 10, Supplementary Table 5)²⁴. DFT calculations also confirmed that the triplet excited state of **1** switched character with the ground state (Supplementary Fig. 11) in terms of reductant-to-oxidant behavior (Supplementary Table 6), and thus is a strong excited-state oxidant (Supplementary Table 7).

Photo-catalytic oxidation of NADH under normoxia

The catalytic photo-oxidation of NADH (3 mM) by **1** (0.25 mM) in H₂O/D₂O/CD₃OD (0.5/49.5/50, v/v, 4 mM NaCl) was monitored by ¹H NMR spectroscopy at 298 K. In the dark, the sample remained unchanged for 24 h. In contrast, ca. 95% of the NADH was oxidised to NAD⁺ after irradiation (463 nm, 30 min), while **1** remained intact (Supplementary Fig. 12).

The photo-catalytic efficiency of **1** (6 μM) towards NADH (240 μM) in PBS was quantified by UV-vis spectroscopy (Supplementary Fig. 13). Upon photoirradiation (463 nm) in air, the absorbance of NADH at 339 nm decreased gradually (Fig. 3a), and the conversion of NADH to NAD⁺ was confirmed by mass spectrometry (Supplementary Fig. 14). A plot of lnA₃₃₉ versus time revealed first-order kinetics with a rate constant *k* of 1.77 × 10⁻² min⁻¹ (Supplementary Fig. 15). The highest observed NADH oxidation turnover number (TON) was 50.2 with a turnover frequency (TOF) of 100.4 h⁻¹ (Supplementary Table 8), much higher than the reported (non-photoactivated) Ir(III) half-sandwich catalyst [(η⁵-Cp^{xbiph})Ir(phpy)py]PF₆ (TOF = 0.83 h⁻¹)²⁷. Moreover, complex **1** was stable during long-term photo-catalysis (2 h, Supplementary Fig. 16). Importantly, the reaction rate was not affected by NaN₃ (¹O₂ scavenger), and was similar in deionised water (Supplementary Fig. 13). After irradiation of **1** and NADH in PBS in air, H₂O₂ was generated as detected by peroxide detection strips (Fig. 3a), and the pH of the reaction solution increased by ca. 2 units (Supplementary Fig. 17).

A Stern–Volmer titration³¹ was used to study the mechanism of NADH photo-catalysis. When the NADH concentration was increased, the phosphorescence intensity of **1** decreased gradually with a dynamic quenching rate coefficient of 6.8 × 10⁶ (Fig. 3b). The phosphorescence lifetime of **1** in air-saturated PBS (330 ns) decreased by ca. 50% after addition of NADH (171 ns, Supplementary Fig. 5).

Electron paramagnetic resonance (EPR) was used to trap radical intermediates during photo-catalytic oxidation of NADH (Fig. 3c) using 5-(2,2-dimethyl-1,3-propoxycyclophosphor-yl)-5-methyl-1-pyrroline-N-oxide (CYPMPO) as the spin trap³². In the presence of CYPMPO, a carbon-centred NAD[•] radical was detected as CYPMPO-NAD together with CYPMPO-CH₃ after irradiation in PBS/methanol (1:1 v/v, 463 nm, 10 min, 293 K). The [•]CH₃ radical was generated by a photo-reaction between H₂O₂ and methanol (Supplementary Fig. 18). Singlet oxygen production was also detected by EPR, and the quantum yield in acetonitrile (0.71) was 7x higher than in PBS ($\Phi = 0.11$; Supplementary Fig. 19). This is due to the longer lifetime of the triplet state in acetonitrile compared to PBS, typical for metal complexes having a triplet excited state^{7,9}.

Molecular adducts of NADH and excited-state ***1** were investigated by DFT calculations. Stable minima were observed for structures with NADH clamped by π - π interactions over the triplet hole orbital localized on the pq ligand (Fig. 3d), and over the triplet particle orbital localized on the ttpy π -system (Fig. 3e), structures which would facilitate electron transport from NADH to ***1**.

Photoreduction of cytochrome c under hypoxia

Under nitrogen, the photo-catalytic activity of **1** decreased significantly (TON = 3.8, Supplementary Fig. 20) due to the absence of a terminal electron acceptor. In the mitochondrial electron transport chain (ETC), the 12.3 kDa heme protein cyt c transfers electrons between Complex III (Coenzyme Q-cyt c reductase) and Complex IV (cyt c oxidase)³³. Release of cyt c from the mitochondria into the cytoplasm induces cell apoptosis³⁴.

The oxidation state of cyt c (Fe²⁺/Fe³⁺) can readily be monitored by the β and α bands at 520 and 550 nm, respectively³⁵. NADH (50 μ M) slowly reduced Fe³⁺-cyt c (11.2 μ M; 293 K, Supplementary Fig. 20). The reaction was slightly accelerated upon 463 nm light irradiation (Supplementary Fig. 21) with low TOF (2.8 h⁻¹, Supplementary Fig. 22). In the absence of

NADH, **1** (0.6 μM) did not reduce Fe^{3+} -cyt c, even under light irradiation (Supplementary Fig. 21). After adding NADH, the rate of photo-reduction of Fe^{3+} -cyt c increased significantly (Fig. 3f), with the TOF increasing to 16.7 h^{-1} . When CYPMPO was added to trap NAD^\bullet , the reduction rate decreased (Supplementary Figs. 21, 22), indicating that NAD^\bullet was involved in Fe^{3+} -cyt c photoreduction.

Photo-cytotoxicity and cell death mechanism

The dark- and photo-cytotoxic activity of **1** was investigated against a range of cancer cell lines, and normal cells MRC-5 (human lung fibroblasts) and LO2 (human hepatocyte cell line), (Supplementary Figs. 23-26, Supplementary Table 9). Cisplatin and 5-aminolevulinic acid (5-ALA) were used as controls (Supplementary Fig. 24). Low dark toxicity was observed for both A549 human lung carcinoma (IC_{50} 43.6 μM) and MRC-5 cells (43.2 μM) after 2 h drug exposure and 46 h recovery. Complex **1** also showed low dark toxicity towards normal LO2 human hepatocyte cells (IC_{50} = 32 μM). For photo-cytotoxicity screening, A549 cells were treated with **1** for 2 h, washed, placed in fresh medium, then irradiated with blue light for 30 min under normoxia (20% O_2 , 465 nm, 8.9 J/cm^2) or hypoxia (1% O_2 , 450 nm, 10 J/cm^2), and left for 46 h to recover. Under normoxia, **1** (1.6 μM) exhibited high photo-cytotoxicity with a photo-cytotoxicity index ($\text{PI} = \text{dark IC}_{50}/\text{light IC}_{50}$) of 27.2. Interestingly, **1** exhibited similar photo-cytotoxicity (dark/light 42.5/2.3 μM , $\text{PI} = 18.5$) under hypoxia. In addition, we found that complex **1** is active against NCI-H460 (lung), HeLa (cervix), Hep G2 (liver) and SGC-7901 (gastric) cancer cell lines upon light irradiation under both 20% and 1% oxygen concentrations with sub-micromolar IC_{50} values (Supplementary Table 9, Supplementary Fig. 23). However, the clinical pro-drug 5-ALA, a precursor of the photosensitizer protoporphyrin, was totally inactive under hypoxia after irradiation (Supplementary Table 9, Supplementary Fig. 24). The photo-cytotoxicity of complex **1** under normoxia was reduced in the presence of NaN_3 ($^1\text{O}_2$ scavenger) and D-mannitol (hydroxyl radical scavenger) for A549 cells. However, these ROS inhibitors had no significant influence on photo-cytotoxicity under hypoxia (Supplementary Fig. 25, Supplementary Table 9), suggesting a different cellular response to photo-catalysis. It should be noted that

cytotoxicity experiments are very sensitive to experimental conditions, including incubation time, irradiation time, light dose, and mode of treatment. Changes in the cytotoxicity of **1**, cisplatin and 5-ALA were observed with change in the incubation time and mode of treatment. As most of complex **1** was taken up by the cells within 2 h of incubation time, in all our photocytotoxicity experiments, 2 h of incubation with **1** was used prior to photoirradiation.

To investigate the phototherapeutic efficiency on a solid tumour model, the photocytotoxicity of **1** towards A549 lung cancer multicellular spheroids (MCS)³⁶ of diameter ca. 800 μm was studied (Supplementary Fig. 27, Supplementary Table 9). Remarkably, using two-photon red light irradiation (760 nm, 12 J/cm²), **1** gave a PI of 9.7 (dark/light 12.6/1.3 μM). Under the same conditions, 5-ALA and cisplatin did not exhibit any significant photocytotoxicity³⁷.

Inductively coupled plasma-mass spectrometry (ICP-MS) confirmed the high cellular uptake of **1** ($162 \pm 6 \text{ ng Ir} \times 10^6 \text{ cells}$, 5 μM treatment, 2 h.). Furthermore, co-localization imaging and quantification by ICP-MS³⁸ (Fig. 4a and Supplementary Fig. 28) showed that ca. 90% of Ir from **1** localized in mitochondria. Importantly, pulsed laser phosphorescence lifetime imaging³⁹ (Fig. 4b) revealed that **1** has an extremely long phosphorescence lifetime in A549 cancer cells (1100 ns, Supplementary Fig. 29).

Next, we investigated photo-induced intracellular NADH depletion in A549 cells. Under normoxia, the intracellular NADH concentration was unaffected after incubation with increasing concentrations of **1** in the dark (Fig. 4c). Upon light irradiation, **1** induced a dramatic depletion in NADH (ca. 4x at 2 μM) and decreased the concentration of adenosine triphosphate (ATP) (Fig. 4d). In addition, the irradiated cells lost their ability to generate formazan from 3-(4,5-dimethylthiazol-2-yl)-2,5-diphenyltetrazolium bromide (MTT), a reaction which requires NAD(P)H-dependent oxidoreductase enzymes (Supplementary Fig. 30)⁴⁰.

We also explored cellular oxidative stress induced by **1**. After light irradiation, a strong green fluorescence was observed from the ROS probe DCFH-DA under both normoxia and hypoxia (Supplementary Fig. 31). A549 lung cancer multicellular spheroid models (ca. 800

µm in diameter) showed that ROS were generated only in the outer regions of the MCS after irradiation with 760 nm two-photon light (Supplementary Fig. 32), indicating the formation of a hypoxic core in the internal region of the spheroids. These results suggested that diffusible ROS species⁴¹ such as H₂O₂ were generated. Indeed, the intracellular H₂O₂ concentration increased ca. 2.5x (Fig. 4e) compared to unexposed cells. Moreover, the cellular H₂O₂ concentration was significantly lower in the presence of N-acetyl-L-cysteine (Fig. 4f), a known ROS scavenger⁴².

A decrease in the mitochondrial membrane potential (MMP) was observed in **1**-treated A549 cells after irradiation under both normoxia and hypoxia (Supplementary Figs. 33, 34), indicating disruption of the mitochondrial ETC⁴³. However, **1** did not induce any significant change in MMP in MRC-5 normal cells in the dark. Furthermore, staining of cells with the green fluorescent FTIC-Annexin V conjugate was observed (Supplementary Fig. 35), indicating cell apoptosis. Moreover, these cells also showed red fluorescence on co-staining with propidium iodide (PI). Apoptotic cells would not allow PI to enter cells, and hence cell death may involve an immunogenic-apoptotic mechanism⁴⁴. We also performed cell membrane calreticulin immunofluorescence and an Enzyme-linked Immunosorbent Assay (ELISA) for high mobility group box 1 protein (HMGB1) (Supplementary Fig. 36). Calreticulin transfer to the outer cell membrane and release of HMGB1 are well known markers of immunogenic cell death⁴⁴. Calreticulin transfer to the outside of the cell membrane, detected by Alexa Fluor 488 linked calreticulin antibody, was observed in the **1**-treated A549 cancer cells upon light irradiation. We also detected release of HMGB1 at the same time. Both these findings, along with the Annexin V /PI assay, confirmed that complex **1** induces immunogenic-apoptotic cell death upon light irradiation.

Discussion

Catalytic metallodrugs activated at low doses have the potential to increase the efficacy of cancer therapy⁴⁵. However, controlling catalytic activity in complicated tissue and cell environments as well as selectivity between normal and cancer cells is extremely challenging.

In contrast to chemotherapy, PDT provides light-directed cancer-cell-targeted treatment and can avoid drug resistance¹². However, cancer cells grow under hypoxia and thus the oxygen-dependent MOA of PDT remains a problem, as is photo-degradation of photosensitisers⁴⁶. Hence we have now designed a stable photo-redox catalyst with an oxygen-independent MOA as a new strategy to overcome these problems.

Our photo-redox catalytic approach recognises two key vulnerabilities in cancer cells. Firstly, the mitochondrial ETC contributes to tumourigenic phenotype amplification, cell proliferation, and especially cell survival under hypoxia²³. Secondly cancer cells are under constant oxidative stress⁴⁷. Coenzyme NADH not only provides electrons for the ETC, but also maintains the cellular redox balance and participates in enzyme reactions²⁴. Photocatalytic NADH depletion and ETC disruption can therefore achieve selective attack on cancer cells and high anticancer activity under hypoxia.

The novel octahedral Ir(III) photocatalyst **1** was synthesised as a single isomer driven by the tridentate ligand ttpy. The X-ray structure and DFT calculations show formation of the *trans* C-Cl isomer, with the negatively-charged C ligand exerting a strong *trans* influence on the Ir-Cl bond. The special ligand coordination architecture tunes the Ir(III) coordination sphere, and ensures well-partitioned HOMO and LUMO within the structure, thus significantly enhancing dark- and photo-stability⁴⁸. In contrast, the Ir(III) photo-catalyst $[\text{Ir}(\text{ppy})_2(\text{bpy})]^+$ (ppy = 2-phenylpyridine, bpy = 2,2'-bipyridine) is not photo-stable and undergoes photodecomposition during long-term light irradiation⁴⁹. Moreover, the presence of a single cyclometalated chelated ligand decreases the electron density at Ir(III), thereby significantly increasing the excited-state redox potential of **1**.

NADH oxidation is usually associated with one-step hydride transfer to substrates, as observed for example in transfer hydrogenation using Cp*-iridium(III) catalysts²⁸. However, initial one-electron transfer is also known⁵⁰, e.g. in thermal reactions of $[\text{Ru}(\text{bpy})_3]^{3+}$ with NADH analogues BNAH (1-benzyl-1,4-dihydronicotinamide)⁵¹, and UVA-induced electron transfer from NADH to generate superoxide for DNA cleavage⁵². Other reports have also used NADH as an electron donor in photosensitisation⁵³; however, electron transfer between a PS and NADH has been little investigated. Our DFT calculations reveal the formation of

“clamped” π - π adducts between excited-state ***1** and NADH which can facilitate photo-induced single electron transfer. As a result, complex **1** achieves high TOF for catalytic NADH oxidation (100.4 h^{-1}) on light irradiation.

The mechanism of the photo-catalytic oxidation of NADH is consistent with the reductive quenching cycle shown in Figure 5. Upon light excitation, the highly oxidative excited state species ***1**(Ir^{III}) extracts an electron from 1,4-dihydronicotinamide, forming a highly reductive **1**(Ir^{II}) species and NADH^{•+} radicals. NADH^{•+} readily deprotonates to generate the neutral carbon-centred NAD[•] radical. Under normoxia (Figure 5a), oxygen oxidises **1**(Ir^{II}) to form superoxide radicals and regenerates **1**(Ir^{III}), completing the photo-catalytic cycle. The superoxide radical extracts an electron from NAD[•] and consumes two protons from the medium as evidenced by the pH increase, forming H₂O₂ and NAD⁺. Under hypoxia, Fe³⁺-cyt c is a terminal electron acceptor (Figure 5b). In previous reports, Ru(II)/Ir(III) bis-terpyridyl complexes and EDTA radicals exhibited a synergistic effect on Fe³⁺-cyt c reduction⁵⁴, whereas here, we discovered that NADH can also serve as a biological electron donor in the synergistic reduction of Fe³⁺-cyt c by complex **1** or the related complex [Ir(tpy)₂]³⁺ (Supplementary Fig. 22). Thus, we confirmed that photo-reduction of Fe³⁺-cyt c can arise from the synergistic action of NAD[•] radicals and the highly reducing Ir^{II} species in a deoxygenated environment. This pathway provides a mechanism for oxygen-independent NADH depletion with its downstream effects on a wide variety of cellular redox enzymes and pathways, and plays an important role in hypoxic photoredox catalysis in cancer cells.

Although mitochondria are dysfunctional in cancer cells, ROS released from the ETC under hypoxia are essential for cancer cell survival and redox regulatory functions⁵⁵. In our system, complex **1** induces significant NADH depletion and ETC disruption only in irradiated cancer cells, as indicated by the MMP decrease under both normoxia and hypoxia. Moreover, ROS generation in cancer cells indicates oxygen consumption during photo-catalysis by **1** which can cut off essential mitochondrion-to-cell redox communication for cell survival under hypoxia⁵⁶. These events lead to the induction of cell apoptosis and necrosis by complex **1**, features of immunogenic apoptosis⁵⁷. Calreticulin immunofluorescence and

HMGB1 ELISA assays confirmed this hypothesis⁴⁴. Immunogenic cell death provides a potentially powerful strategy for anticancer therapy⁵⁸, reinstating the body's defense against cancer.

In addition, both DFT calculations and experimental data reveal strong near infrared two-photon absorption of **1**, and we have demonstrated promising phototherapeutic effects on A549 multicellular lung cancer spheroids. These one-photon and two-photon light activation properties of **1** will facilitate a broad application from superficial lesions to solid tumours.

Conclusions

We report for the first time both aqueous and in-cell photo-catalytic oxidation of coenzyme NADH by a metal complex, with a very high TOF. The novel octahedral cyclometalated Ir^{III} photoredox catalyst, complex **1**, is highly photostable with a long phosphorescence lifetime. This catalyst, with its unusually high excited state redox potential, not only generates NAD[•] radicals, but also perturbs electron transfer pathways in mitochondria by reduction of Fe³⁺-cytochrome c, inducing redox imbalance in cancer cells. The photoredox catalyst is equipotent towards normoxic and hypoxic adherent cancer cells, disrupting the mitochondrial membrane potential and inducing immunogenic apoptotic cell death. In contrast, current clinical photo-chemotherapeutic agents are less effective in hypoxic environments. Moreover, photo-catalyst **1** exhibits low toxicity towards normal cells in the dark, a favorable profile for reducing the side-effects of treatment. Complex **1** with its photo-controlled oxygen-independent immunogenic-apoptotic mechanism of cancer cell death is promising for further evaluation as a novel targeted anticancer agent.

Methods

UV-vis studies of complex 1 and NADH reactions. Reactions between complex **1** and NADH in various mol ratios were monitored by UV-vis spectroscopy at 310 K in the dark and on irradiation with 463 nm light. Turnover number (TON) is defined as the number of moles of NADH that a mole of complex **1** can convert within 30 min. Turnover frequency (TOF) was calculated from the difference in NADH concentration after 30 min divided by the

concentration of complex **1**. The concentration of NADH was obtained using the extinction coefficient $\epsilon_{339} = 6220 \text{ M}^{-1}\text{cm}^{-1}$.

Electron paramagnetic resonance (EPR). EPR spectra were recorded at ambient temperature (ca. 293 K) on a Bruker Model A300 ESR spectrometer equipped with a Bruker ER 4122 SHQ resonator using 1.0 mm quartz tubes. Typical instrument settings were: modulation amplitude 2.0 G and microwave power 0.63 mW, X-band frequency ca. 9.88 GHz. Spectra were acquired at 20 dB microwave attenuation (non-saturating 2 mW microwave power) with modulation amplitude of 0.2 mT peak-to-peak, time constant of 1.28 ms, receiver gain, 50–200; sweep time, 30 s and conversion time of 5.12 ms. The spin trap 5-(2,2-dimethyl-1,3-propoxycyclo-phosphoryl)-5-methyl-1-pyrroline N-oxide (CYPMPO 1 mM) was used for NAD^\bullet radicals in PBS/methanol (1:1 v/v) containing complex **1** (500 μM , methanol) and NADH (10 mM, PBS) under 463 nm irradiation.

Electrochemistry

Cyclic voltammograms were recorded using a CH Instrument model 600D Electrochemical Analyzer/Workstation (Austin, TX). The electrochemical measurements were performed on complex **1** (1.0 mM) in acetonitrile solutions containing tetrabutylammonium hexafluorophosphate (0.1 M) as supporting electrolyte. The solutions were degassed under nitrogen and cyclic voltammograms were scanned from -2.3 V to +2.3 V (three complete scans for each experiment). In a typical electrochemical experimental set up, a three-electrode system was used: a glassy carbon electrode as the working electrode, Ag/AgCl in 3.0 M KCl as the reference electrode, and platinum wire as the counter electrode. CV was performed at a scan rate of 100 mV/s. The excited state redox potentials were calculated from the ground state redox potentials and the emission maxima to aid evaluation of the photosensitization properties of complex **1**. Excited state reductive potentials: $E([\text{M}^*]^+ / [\text{M}]^{2+}) = E_{\text{ox}} - E_{\lambda\text{em}}$. Excited state oxidative potentials: $E([\text{M}^*]^+ / [\text{M}]^0) = E_{\text{red}} + E_{\lambda\text{em}}$. $E_{\lambda\text{em}} = 1240 \text{ eV nm} / \lambda_{\text{em}}$.

Data availability

The data that support the findings of this study are available within the paper and its Supplementary Information files, or from the corresponding authors on reasonable request. Crystallographic data for the complex [1]PF₆·(1.5 toluene) reported in this Article have been deposited at the Cambridge Crystallographic Data Centre, under deposition numbers CCDC 1840366). After the Open Access agreement has been established, underpinning datasets will be deposited in Warwick's Institutional Repository: Warwick Research Archive Portal (WRAP), according to the Open Access Agreement.

References

1. Riddell, I. A. & Lippard, S. J. Cisplatin and oxaliplatin: Our current understanding of their actions. *Met Ions Life Sci.* **18**, 1-42 (2018).
2. Meier-Menches, S. M. Gerner, C. Berger, W. Hartinger, C. G. & Keppler, B. K. Structure–activity relationships for ruthenium and osmium anticancer agents–towards clinical development. *Chem. Soc. Rev.* **47**, 909-928 (2018).
3. Bergamo, A. Dyson, P. J. & Sava, G. The mechanism of tumour cell death by metal-based anticancer drugs is not only a matter of DNA interactions. *Coord. Chem. Rev.* **360**, 17-33 (2018).
4. Farrer, N. J. Salassa, L. & Sadler, P. J. Photoactivated chemotherapy (PACT): the potential of excited-state d-block metals in medicine. *Dalton Trans.* **48**, 10690-10701 (2009).
5. Banerjee, S. & Chakravarty, A. R. Metal complexes of curcumin for cellular imaging, targeting, and photoinduced anticancer activity. *Acc. Chem. Res.* **48**, 2075-2083 (2015).
6. Lo, K. K. W. Luminescent rhenium(I) and iridium(III) polypyridine complexes as biological probes, imaging reagents, and photocytotoxic agents. *Acc. Chem. Res.* **48**, 2985-2995 (2015).
7. Knoll, J. D. & Turro, C. Control and utilization of ruthenium and rhodium metal complex excited states for photoactivated cancer therapy. *Coord. Chem. Rev.* **282**, 110-126 (2015).
8. Liu, J. *et al* Harnessing ruthenium(II) as photodynamic agents: Encouraging advances in cancer therapy. *Coord. Chem. Rev.* **363**, 17-28 (2018).
9. Heinemann, F. Karges, J. & Gasser, G. Critical overview of the use of Ru (II) polypyridyl complexes as photosensitizers in one-photon and two-photon photodynamic therapy. *Acc. Chem. Res.* **50**, 2727-2736, (2017).
10. Shi, G. *et al*. Ru(II) dyads derived from α -oligothiophenes: A new class of potent and versatile photosensitizers for PDT. *Coord. Chem. Rev.* **282**, 127-138 (2015).
11. Meggers, E. Asymmetric catalysis activated by visible light. *Chem. Commun.* **51**, 3290-3301 (2015).
12. Spring, B. Q. Rizvi, I. Xu, N. & Hasan, T. The role of photodynamic therapy in

- overcoming cancer drug resistance. *Photochem. Photobiol. Sci.* **14**, 1476-1491 (2015).
13. Teicher, B. A. Hypoxia and drug resistance. *Cancer Metast. Rev.* **13**, 139-168 (1994).
 14. Wang, H. P. *et al.* Phospholipid hydroperoxide glutathione peroxidase protects against singlet oxygen-induced cell damage of photodynamic therapy, *Free Radical Biol. Med.* **30** 825–835 (2001).
 15. Henderson, B. & Miller, A. Effects of scavengers of reactive oxygen and radical species on cell survival following photodynamic treatment *in vitro*: comparison to ionizing radiation. *Radiat. Res.* **108**, 196-205 (1986).
 16. Gomer, C. *et al.* Photodynamic Therapy-mediated oxidative stress can induce the expression of heat shock proteins. *Cancer Res.* **56**, 2355-2360 (1996).
 17. Ruhdorfer, S. Sanovic, R. Sander, V. Krammer, B. & Verwanger, T. Gene expression profiling of the human carcinoma cell line A-431 after 5-aminolevulinic acid-based photodynamic treatment. *Int. J. Oncol.* **30**, 1253-1262 (2007).
 18. Tong, Z. Singh, G. & Rainbow, A. J. Sustained activation of the extracellular signal regulated kinase pathway protects cells from photofrin-mediated photodynamic therapy. *Cancer Res.* **62**, 5528-5535 (2002).
 19. Edmonds, C. Hagan, S. Gallagher-Colombo, S. M. Busch, T. M. & Cengel, K. A. Photodynamic therapy activated signaling from epidermal growth factor receptor and STAT3: Targeting survival pathways to increase PDT efficacy in ovarian and lung cancer, *Cancer Biol. Ther.* **13**, 1463-1470 (2012).
 20. Assefa, Z. *et al.* The activation of the c-Jun N-terminal kinase and p38 mitogen-activated protein kinase signaling pathways protects HeLa cells from apoptosis following photodynamic therapy with hypericin, *J. Biol. Chem.* **274**, 8788–8796 (1999).
 21. Kessel, D. & Erickson, C. Porphyrin photosensitization of multi-drug resistant cell types. *Photochem. Photobiol.* **55**, 397-399 (1992).
 22. Hockel, M. & Vaupel, P. Tumor hypoxia: definitions and current clinical, biologic, and molecular aspects. *J. Natl. Cancer Inst.* **93**, 266-276 (2001).
 23. Klimova, T. & Chandel, N. S. Mitochondrial complex III regulates hypoxic activation of HIF. *Cell Death Differ.* **15**, 660-666 (2008).

24. Chiarugi, A. Dölle, C. Felici, R. & Ziegler, M. The NAD metabolome-a key determinant of cancer cell biology. *Nat. Rev. Cancer* **12**, 741-752 (2012).
25. Prier, C. K. *et al.* Visible light photoredox catalysis with transition metal complexes: applications in organic synthesis. *Chem. Rev.* **113**, 5322-5363 (2013).
26. Huo, H. *et al.* Asymmetric photoredox transition-metal catalysis activated by visible light. *Nature* **515**, 100-103 (2014).
27. Demas, J. N. *et al.* Peer Reviewed: Oxygen Sensors Based on Luminescence Quenching. *Anal. Chem.* **71**, 793A-800A (1999).
28. Liu, Z. *et al.* The potent oxidant anticancer activity of organoiridium catalysts. *Angew. Chem. Int. Ed.* **53**, 3941-3946 (2014).
29. Ma, J. *et al.* Preparation of chiral-at-metal catalysts and their use in asymmetric photoredox chemistry. *Nat. Protoc.* **13**, 605-632 (2018).
30. Peterson, J. R. Smith, T. A. & Thordarson, P. Synthesis and room temperature photo-induced electron transfer in biologically active bis (terpyridine) ruthenium(II)-cytochrome c bioconjugates and the effect of solvents on the bioconjugation of cytochrome c. *Org. Biomol. Chem.* **8**, 151-162 (2010).
31. Boaz, H. & Rollefson, G. K. The quenching of fluorescence. Deviations from the Stern-Volmer law. *J. Am. Chem. Soc.* **72**, 3435-3443 (1950).
32. Matsuzaki, S. Kotake, Y. & Humphries, K. M. Identification of mitochondrial electron transport chain-mediated NADH radical formation by EPR spin-trapping techniques. *Biochemistry* **50**, 10792-10803 (2011).
33. Lapuente-Brun, E. *et al.* Supercomplex assembly determines electron flux in the mitochondrial electron transport chain. *Science* **340**, 1567-1570 (2013).
34. Li, H. *et al.* Cytochrome c release and apoptosis induced by mitochondrial targeting of nuclear orphan receptor TR3. *Science*, **289**, 1159-1164 (2000).
35. Margoliash, E. & Frohwirt, N. Spectrum of horse-heart cytochrome c. *Biochem. J.* **71**, 570-572 (1959).
36. Huang, H. *et al.* Highly charged ruthenium(ii) polypyridyl complexes as lysosome-localized photosensitizers for two-photon photodynamic therapy. *Angew. Chem. Int. Ed.*

- 54**, 14049-14052 (2015).
37. Peng, Q. *et al.* 5-Aminolevulinic acid-based photodynamic therapy. *Cancer* **79**, 2282-2308 (1997).
 38. Huang, H. *et al.* Real-time tracking mitochondrial dynamic remodeling with two-photon phosphorescent iridium(III) complexes. *Biomaterials* **83**, 321-331 (2016).
 39. Berezin, M. Y. & Achilefu, S. Fluorescence lifetime measurements and biological imaging. *Chem. Rev.* **110**, 2641-2684 (2010).
 40. Berridge, M. V. Herst, P. M. & Tan, A. S. Tetrazolium dyes as tools in cell biology: new insights into their cellular reduction. *Biotechnol. Annu. Rev.* **11**, 127-152 (2005).
 41. Waghray, M. *et al.* Hydrogen peroxide is a diffusible paracrine signal for the induction of epithelial cell death by activated myofibroblasts. *FASEB J.* **19**, 854-856 (2005).
 42. He, Y. Y. & Häder, D. P. UV-B-induced formation of reactive oxygen species and oxidative damage of the cyanobacterium *Anabaena* sp.: protective effects of ascorbic acid and N-acetyl-L-cysteine. *J. Photochem. Photobiol. B* **66**, 115-124 (2002).
 43. Ricci, J. E. *et al.* Disruption of mitochondrial function during apoptosis is mediated by caspase cleavage of the p75 subunit of complex I of the electron transport chain. *Cell*, **117**, 773-786 (2004).
 44. Tesniere, A. *et al.* Immunogenic death of colon cancer cells treated with oxaliplatin. *Oncogene* **29**, 482-491 (2010).
 45. Coverdale, J. P. *et al.* Asymmetric transfer hydrogenation by synthetic catalysts in cancer cells. *Nat. Chem.* **10**, 347-354 (2018).
 46. Moan, J. Effect of bleaching of porphyrin sensitizers during photodynamic therapy. *Cancer lett.* **33**, 45-53 (1986).
 47. Gorrini, C. Harris, I. S. & Mak, T. W. Modulation of oxidative stress as an anticancer strategy. *Nat. Rev. Drug Discov.* **12**, 931-947 (2013).
 48. Porras, J. A. Mills, I. N. Transue, W. J. & Bernhard, S. Highly Fluorinated Ir(III)-2,2':6',2''-Terpyridine-Phenylpyridine-X Complexes via Selective C-F Activation: Robust Photocatalysts for Solar Fuel Generation and Photoredox Catalysis. *J. Am. Chem. Soc.* **138**, 9460-9472 (2016).

49. Tinker, L. L. *et al.* Visible light induced catalytic water reduction without an electron relay. *Chem. Eur. J.* **13**, 8726-8732 (2007).
50. Gębicki, J. Marcinek, A. & Zielonka, J. Transient species in the stepwise interconversion of NADH and NAD⁺. *Acc. Chem. Res.* **37**, 379-386 (2004).
51. Fukuzumi, S. Inada, O. & Suenobu, T. Mechanisms of electron-transfer oxidation of NADH analogues and chemiluminescence. Detection of the keto and enol radical cations. *J. Am. Chem. Soc.* **125**, 4808-4816 (2003).
52. Tanaka, M. Ohkubo, K. & Fukuzumi, S. DNA cleavage by UVA irradiation of NADH with dioxygen via radical chain processes. *J. Phys. Chem. A* **110**, 11214-11218 (2006).
53. Lee, H. Y. Chen, S. Zhang, M. H. & Shen, T. Studies on the synthesis of two hydrophilic hypocrellin derivatives with enhanced absorption in the red spectral region and on their photogeneration of O₂⁻ and O₂(¹Δ_g). *J. Photochem. Photobiol. B* **71**, 43-50 (2003).
54. Hvasanov, D. Mason, A. F. Goldstein, D. C. Bhadbhade, M. & Thordarson, P. Optimising the synthesis, polymer membrane encapsulation and photoreduction performance of Ru(II)-and Ir(III)-bis(terpyridine) cytochrome c bioconjugates. *Org. Biomol. Chem.* **11**, 4602-4612 (2013).
55. Sabharwal, S. S. & Schumacker, P. T. Mitochondrial ROS in cancer: initiators, amplifiers or an Achilles' heel? *Nat. Rev. Cancer* **14**, 709-721 (2014).
56. Wenzel, C. *et al.* 3D high-content screening for the identification of compounds that target cells in dormant tumor spheroid regions. *Exp. Cell Res.* **323**, 131-143 (2014).
57. Ji, J. Zhang, Y. Chen, W. R. Wang, X. DC vaccine generated by ALA-PDT-induced immunogenic apoptotic cells for skin squamous cell carcinoma. *Oncoimmunology* **5**, e1072674 (2016).
58. Galluzzi, L. Buqué, A. Kepp, O. Zitvogel, L. & Kroemer, G. Immunogenic cell death in cancer and infectious disease. *Nat. Rev. Immunol.* **17**, 97-111 (2017).

Acknowledgements

We thank the EPSRC (grants EP/G006792, EP/F034210/1 and EP/P030572/1 for P.J.S., platform grant EP/P001459/1 for M.J.P, EPSRC DTP studentship for T.M., EP/N010825/1

for M.S., and EP/N010825 for V.G.S.), MRC (grant G0701062 for P.J.S.), The Royal Society (Newton International Fellowship NF160307 for H.H., Newton-Bhabha International Fellowship NF151429 for S.B.), Leverhulme Trust (Senior Research Fellowship for V.G.S.), National Science Foundation of China (grants NSFC, 21701113 for P.Z., 21525105, 21471164, 21778079 for H.C.), 973 Program (2015CB856301 for H.C.), The Fundamental Research Funds for the Central Universities (for H.C.), ERC (Consolidator Grant GA 681679 PhotoMedMet for G.G.), and French Government (Investissementsd'Avenir grant ANR-10-IDEX-0001-02 PSL for G.G.). The Sun Yat-sen University Startup fund 75110-18841213 for H.H. We also thank W. Zhang, Dr. L. Song and P. Aston for assistance with mass spectrometry; Dr. J. P. C. Coverdale for assistance with ICP-MS experiments; and Dr. I. Prokes for assistance with NMR spectroscopy.

Correspondence and requests for materials should be addressed to P. J. S. (p.j.sadler@warwick.ac.uk), H. C. (ceschh@mail.sysu.edu.cn) or G. G. (gilles.gasser@chimieparistech.psl.eu)

Author Contributions

All authors were involved with the design and interpretation of experiments and with the writing of the script. H. H. and S. B. contributed equally to this work. Chemical and biological experiments were carried out by H. H., S. B., K. Q. and P.Z. X-ray crystallography was carried out by S. B. and G. J. C. DFT calculations were carried by O. B., T. M. and M. J. P. M. S. and V. G. S. carried out the excited state photochemistry experiments and analyzed the data. H. H., S. B., H. C., G. G. and P. J. S analyzed the data and co-wrote the paper. All authors discussed the results and commented on the manuscript. All authors have given approval to the final version of the manuscript.

Competing interests

The authors declare no competing interests.

Additional information

***e-mail:**

Supplementary Information is available with the online version of this paper.

Figure Captions

Figure 1. Structures and stability of compounds. a) NADH. b) Complex **1**, line structure, and c) X-ray crystal structure; the counter ion PF_6^- has been omitted for clarity.

Figure 2. DFT calculations and stability of complex 1. a) Dominant canonical particle-hole orbitals with overall contribution to the lowest first triplet state of **1**. b) Dominant canonical particle-hole orbital representation of the strong TPA intermediate state by non-resonant 3-state model. c) UV-vis spectra showing the dark stability of **1** in RPMI-1640 cell culture medium at 293 K for 24 h. The experiment was repeated three times independently with similar results. d) Photostability of the emission of **1** in PBS under continuous 463 nm light irradiation for 30 min at 293 K. The experiment was repeated three times independently with similar results.

Figure 3 Photoredox reaction between NADH and complex 1 under 463 nm blue-light irradiation. a) Photo-catalytic oxidation of NADH (240 μM) by complex **1** (6 μM) in PBS monitored by UV-vis spectroscopy; inset: detection of H_2O_2 after irradiation (D = dark, L = light). The experiment was repeated five times independently with similar results. b) Stern–Volmer plot showing NADH interacts with the excited state of complex **1**. The experiment was repeated three times independently with similar results. c) X-band EPR spectrum of NAD^\bullet radicals trapped by CYPMPO at various times after irradiation with 463 nm light: CYPMPO-NAD (blue circles, $\alpha_{\text{N}} = 14.43$ G, $\alpha_{\text{H}} = 20.35$ G, $\alpha_{\text{P}} = 50.72$ G), CYPMPO- CH_3 (red circles, $\alpha_{\text{N}} = 14.67$ G, $\alpha_{\text{H}} = 20.25$ G, $\alpha_{\text{P}} = 48.92$ G). The experiment was repeated five times independently with similar results. d) Optimized DFT stable minima for NADH-**1** (triplet state) structures with NADH clamped around pq or e) ttpy ligands. f) Photo-

catalytic reduction of oxidised cyt c (11.2 μM) by NADH (50 μM) and complex **1** (0.6 μM), inset: dependence of absorbance at 550 nm on irradiation time. The experiment was repeated three times independently with similar results.

Figure 4 Cellular localization and cellular response after irradiation. a) One- and two-photon images of A549 lung cancer cells treated with **1** (5 μM) for 1 h and co-stained with mitochondrial and lysosomal dyes. $\lambda_{\text{ex}}/\lambda_{\text{em}}$: **1** 405/562 nm, lysotracker 488/520 nm, mitotracker 633/660 nm. The experiment was repeated three times independently with similar results. b) Phosphorescence lifetime images of living A549 living cells treated with **1** (5 μM), $\lambda_{\text{ex}}/\lambda_{\text{em}}$: 760/562 nm. The experiment was repeated twice independently with similar results. c) NADH concentration, d) ATP concentration, and e) H_2O_2 concentration, in A549 cells treated with various doses of **1** in the dark or light. f) H_2O_2 concentration in A549 cells after light irradiation in the presence or absence of 5 mM N-acetyl-L-cysteine (NAC; cell exposure to **1** for 2 h, washed, followed by 465 nm light irradiation 8.9 J/cm^2). RLU: relative luminescence unit. Figure 4c-4f: All the experiments were performed as duplicates of triplicates ($n=6$ biologically independent experiments). Error bars show ± 1 s.d. from the mean. Statistics were calculated using the two-tailed t-test with unequal variances (Welch's unpaired t-test) by comparing sample treated with the same dose in the presence or absence of light irradiation. * $p < 0.05$, ** $p < 0.01$ *** $p < 0.001$. p values:
4c: NADH 0.5 μM ($p = 0.0029$), 1.0 μM ($p = 0.0003$), 2.0 μM ($p = 0.0002$)
4d: ATP light 1.0 μM ($p = 0.0132$), 2.0 μM ($p = 0.0052$)
4e: H_2O_2 0.5 μM ($p = 0.0048$), 1.0 μM ($p = 0.0025$), 2.0 μM ($p = 0.0009$)
4f: +NAC 0.0 μM ($p = 0.0009$), 0.5 μM ($p = 0.0003$), 1.0 μM ($p = 0.0035$), 2.0 μM ($p = 0.0003$).

Figure 5. Photo-catalytic cycle for oxidation of NADH by complex 1 showing the production of NAD^\cdot radicals, involvement of oxygen, and reduction of cytochrome c. a) The reductive catalytic cycle under normoxia. b) Catalytic cycle under hypoxia in the presence of Fe^{3+} -cyt c as electron acceptor.

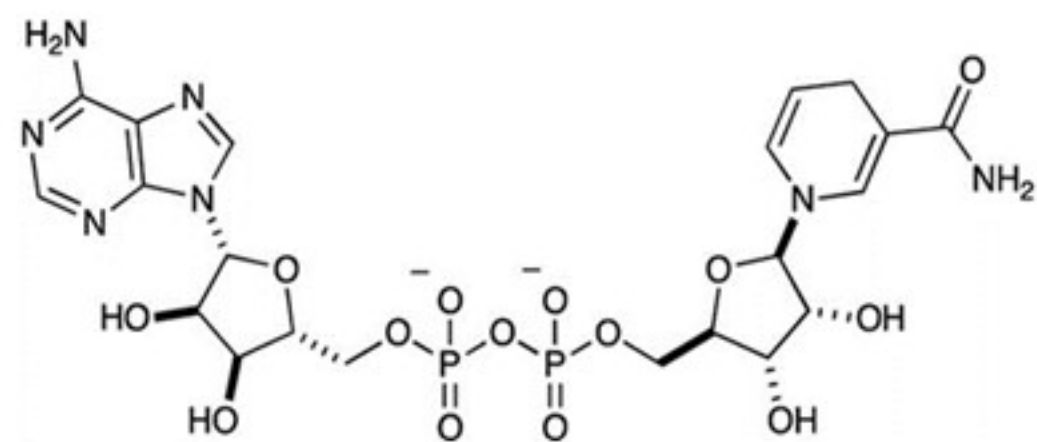
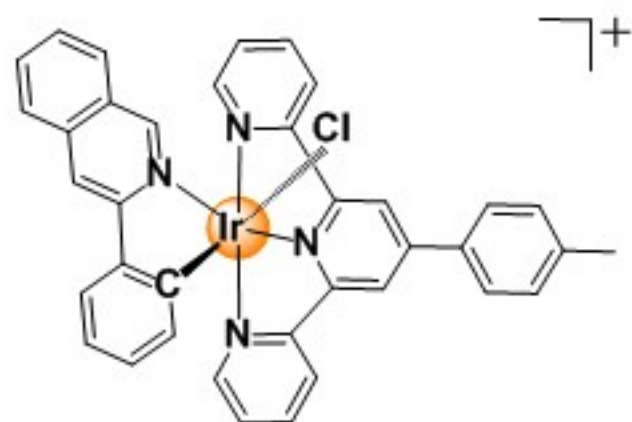
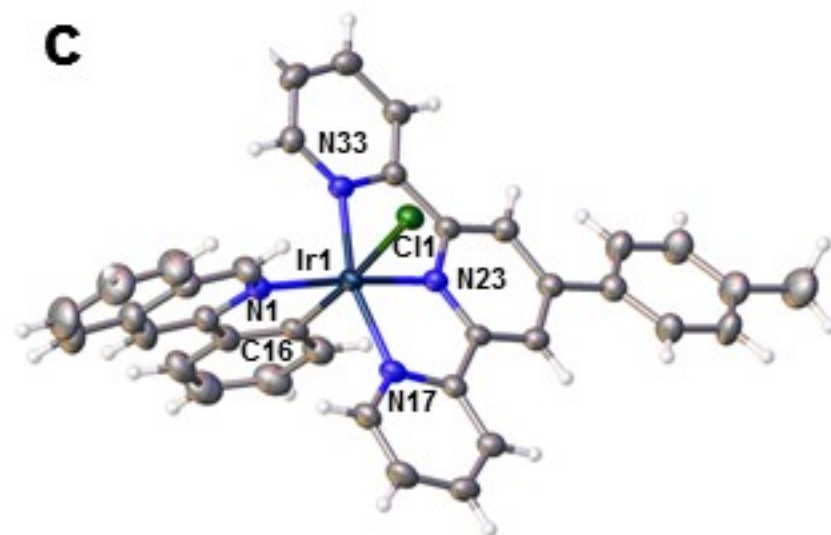
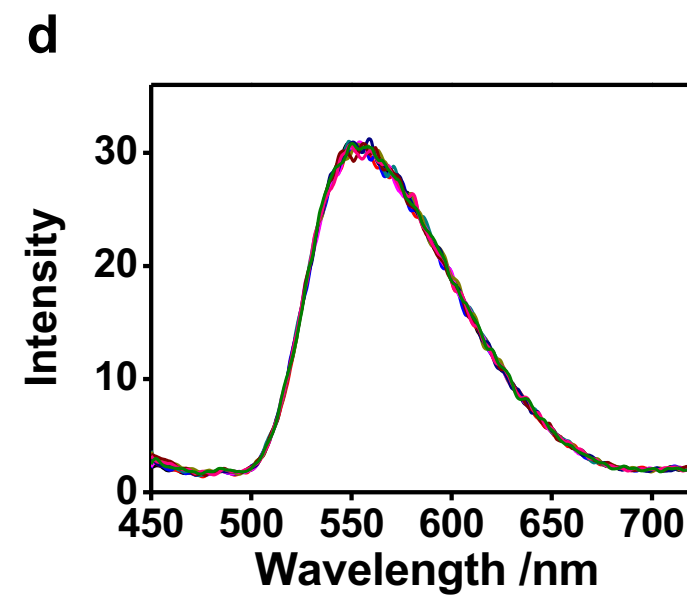
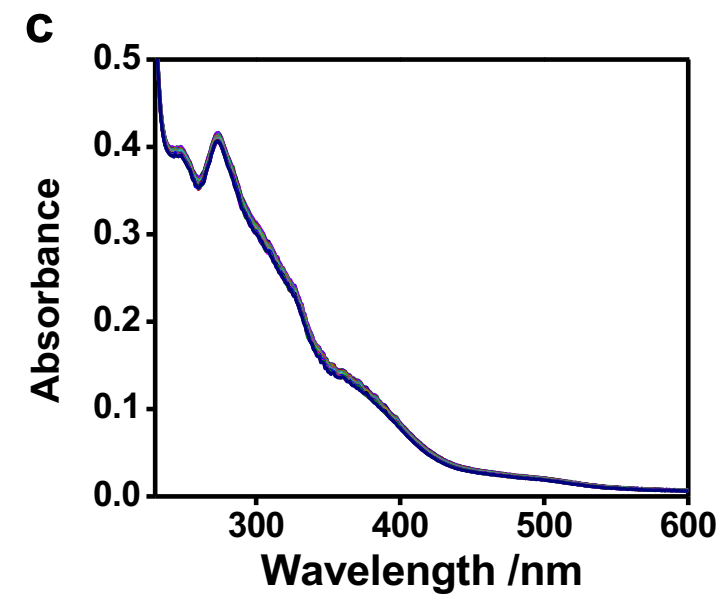
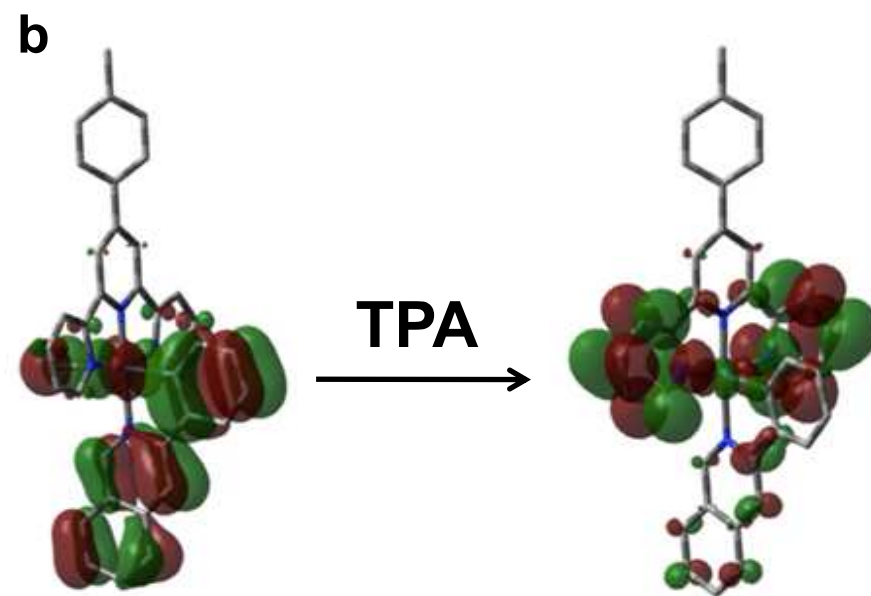
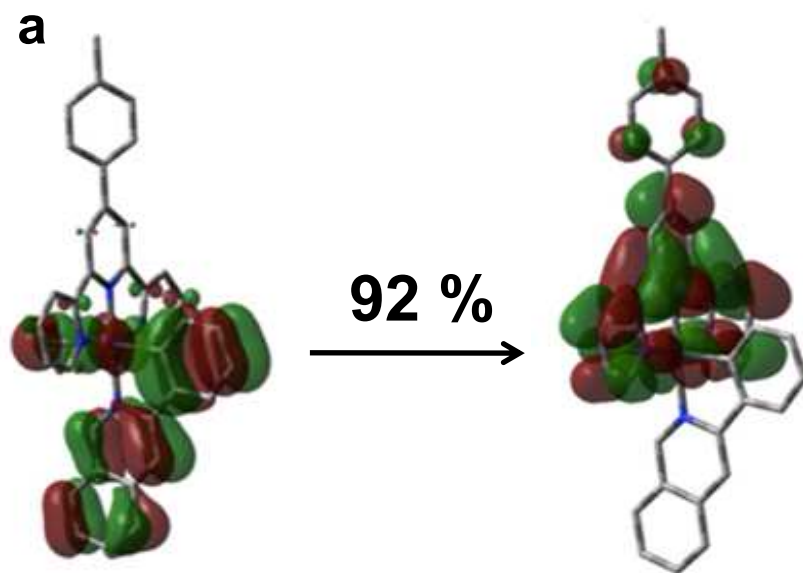
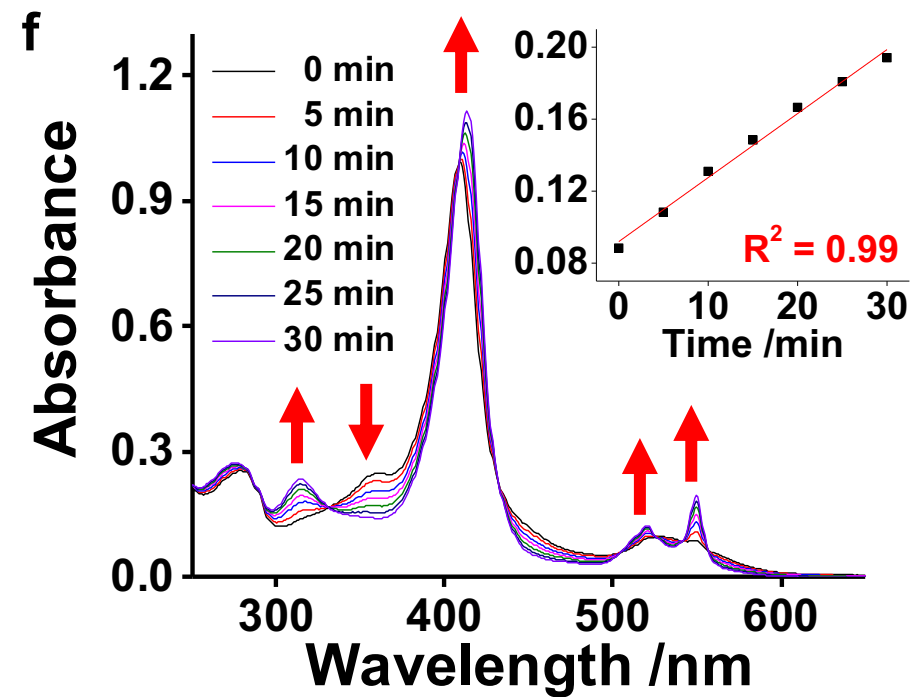
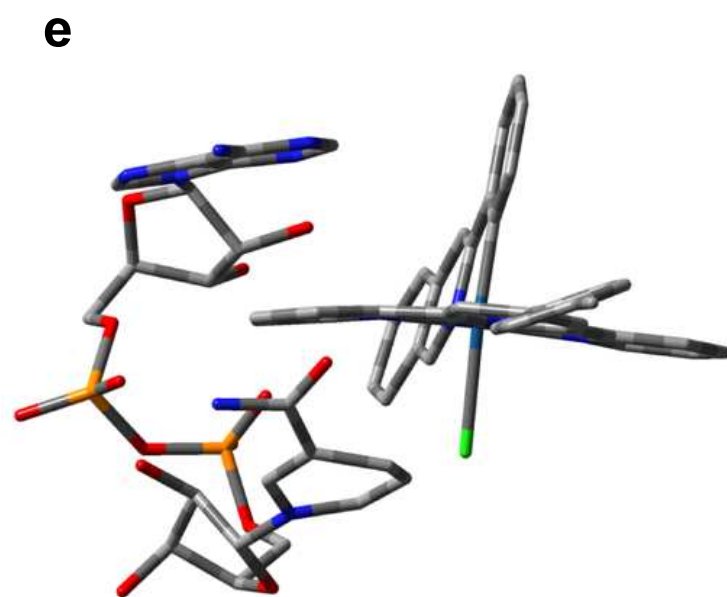
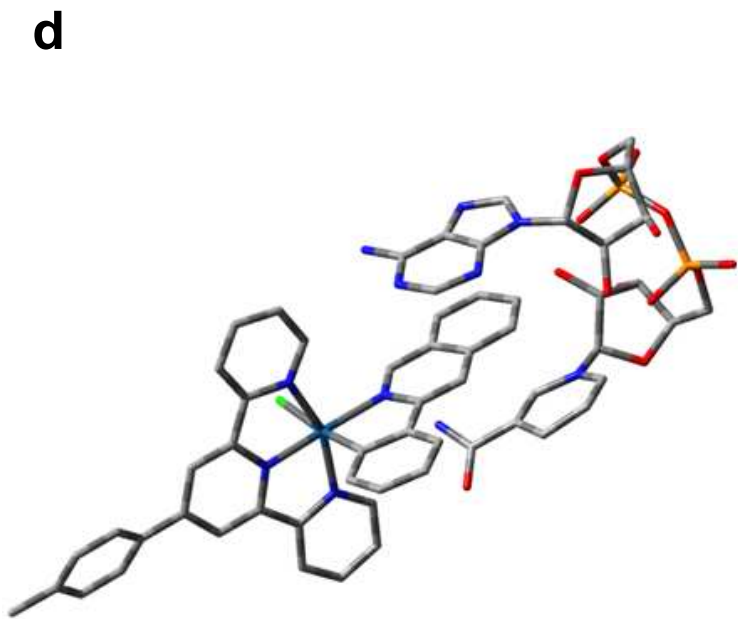
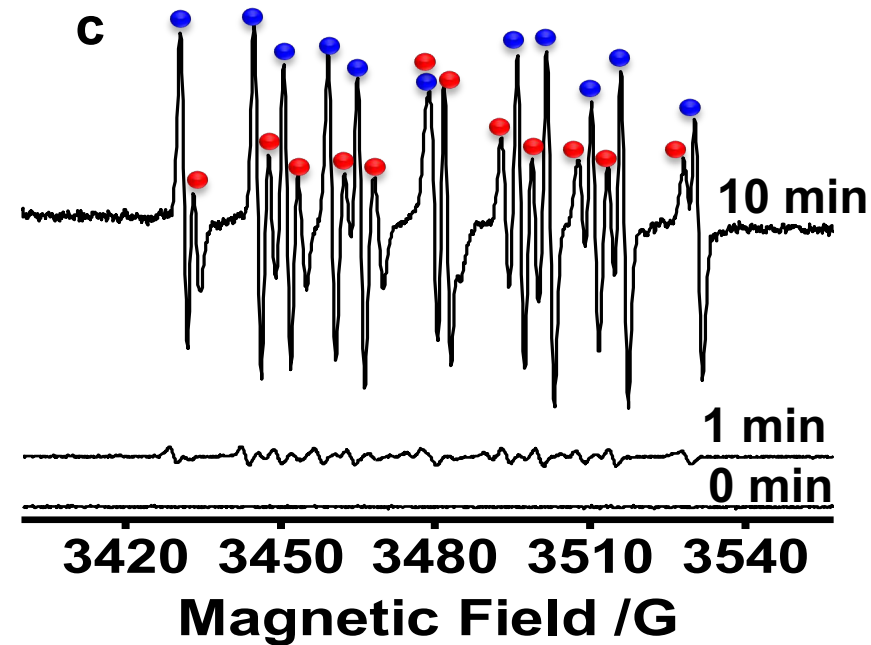
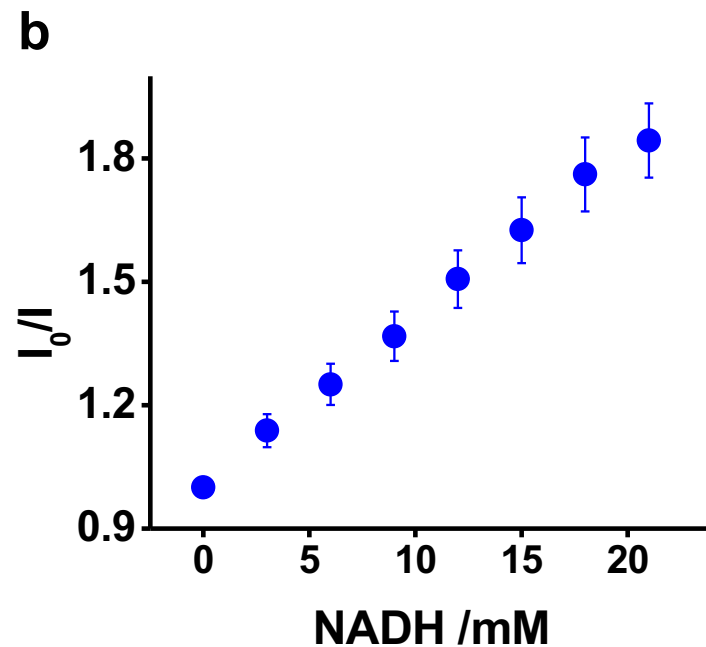
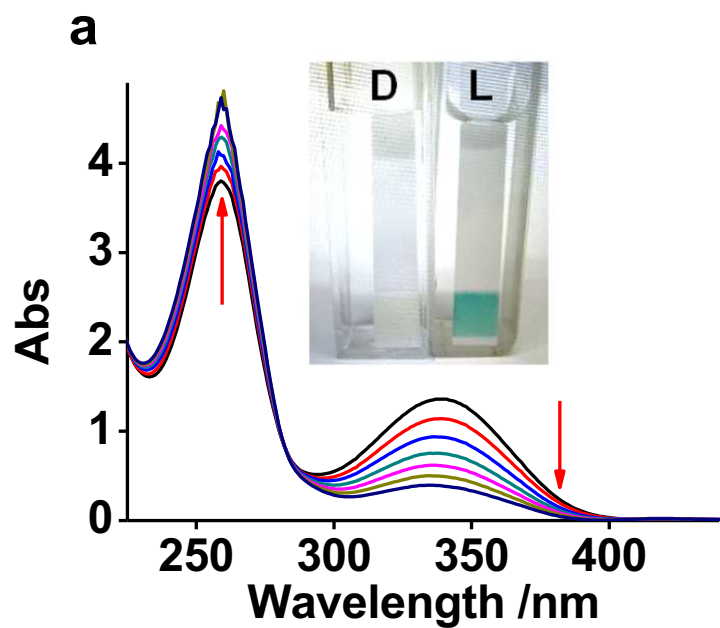
a**NADH****b****c**

Figure 2





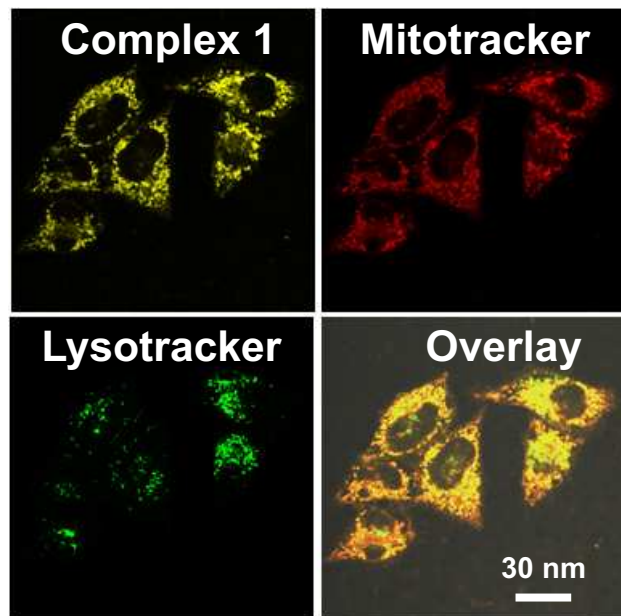
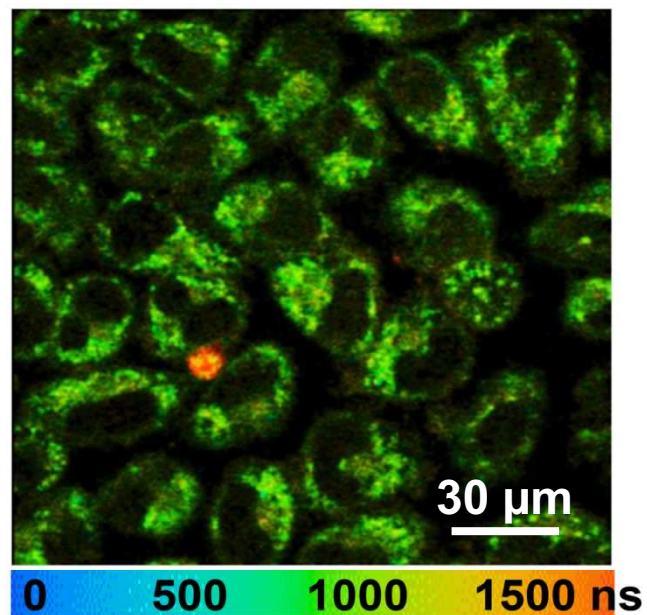
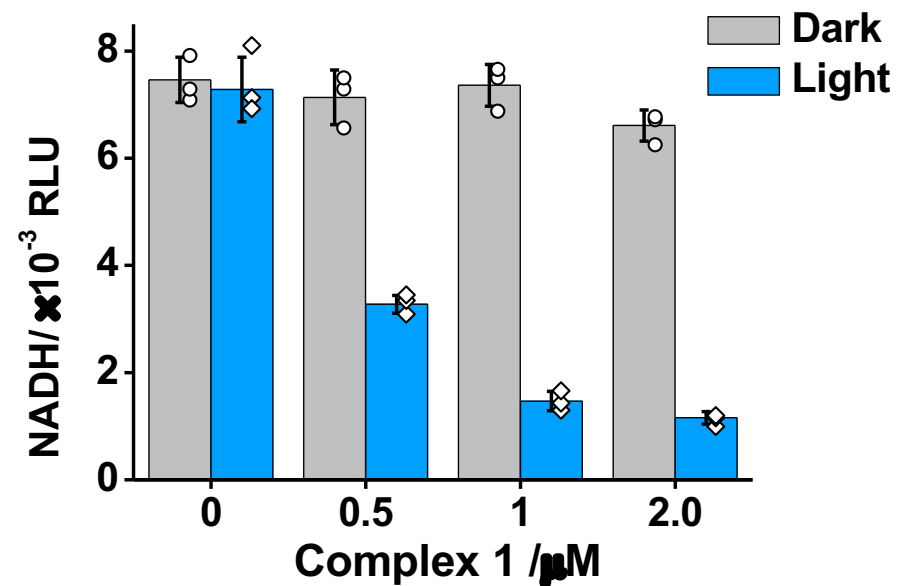
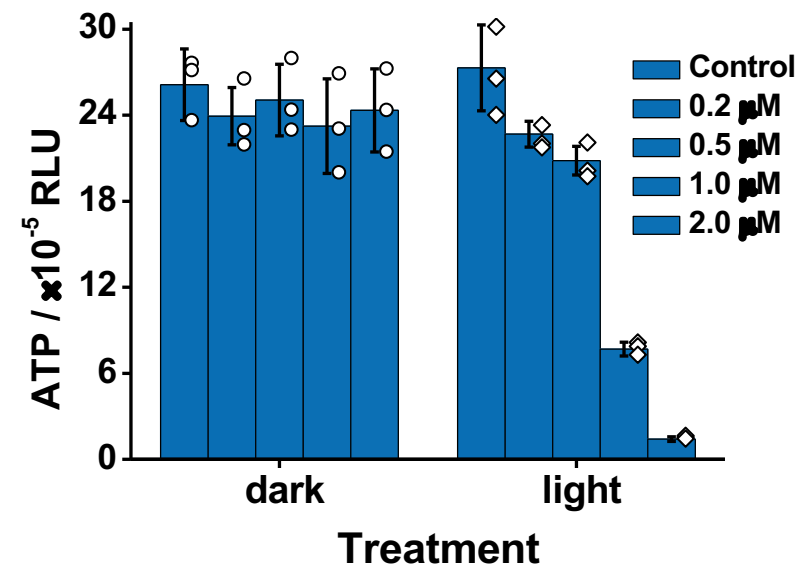
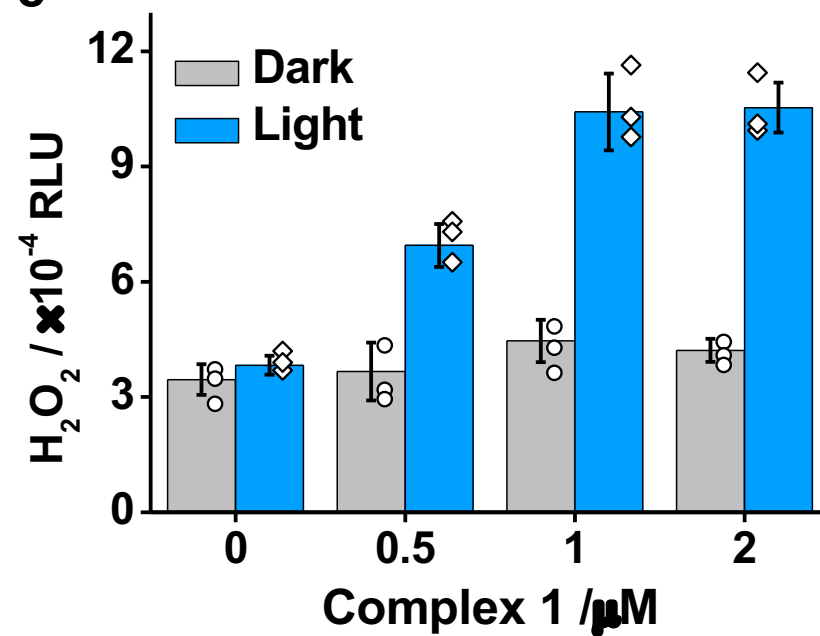
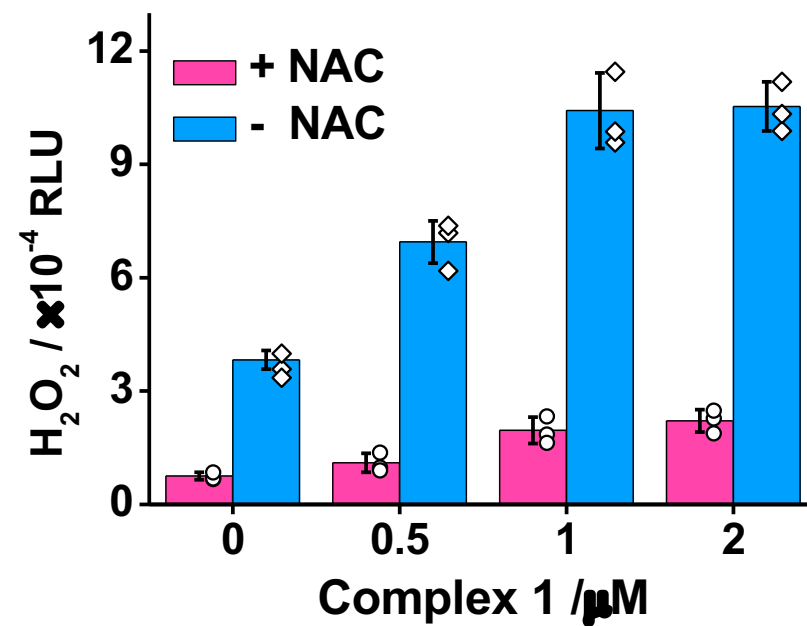
a**b****c****d****e****f**

Figure 5

